Simulations of Seismic Wave Propagation on Mars

Bodzag, Ebru; Ruan, Youyi; Metthez, Nathan; Khan, Amir; Leng, Kuangdai; Van Driel, Martin; Wieczoreck, Mark; Rivoldini, Attilio; Larmat, Carene; Giardini, Domenico; Tromp, Jeroen; Lognonne, Philippe; Banerdt, Bruce

Simulations of seismic wave propagation on Mars

Ebru Bozdağ · Youyi Ruan · Nathan
Metthez · Amir Khan · Kuangdai
Leng · Martin van Driel · Mark
Wieczorek · Attilio Rivoldini · Carène
S. Larmat · Domenico Giardini · Jeroen
Tromp · Philippe Lognonné · Bruce W.
Banerdt

E. Bozdağ
Université Côte d'Azur, CNRS-OCA-IRD-Géoazur, Valbonne, France
Tel.: +33 4 83 61 86 47
E-mail: bozdag@geoazur.unice.fr

Y. Ruan
Princeton University, Princeton, NJ, USA

N. Metthez
ETH Zurich, Zurich, Switzerland

A. Khan
ETH Zurich, Zurich, Switzerland

K. Leng
University of Oxford, Oxford, UK

M. van Driel
ETH Zurich, Zurich, Switzerland

M. Wieczorek
Université Côte d'Azur, Observatoire de la Côte d'Azur, CNRS, Laboratoire Lagrange, Nice,
France

A. Rivoldini
Royal Observatory of Belgium, Brussels, Belgium

C. S. Larmat
Los Alamos National Laboratory, NM, USA

D. Giardini
ETH Zurich, Zurich, Switzerland

J. Tromp
Princeton University, Princeton, NJ, USA

P. Lognonné
Institut de Physique du Globe de Paris-Sorbonne Paris Cité, Université Paris Diderot, Paris,
France

B. W. Banerdt
Jet Propulsion Laboratory, California Institute of Technology, Pasadena, CA, USA

Abstract We present global and regional synthetic seismograms computed for 1D and 3D Mars models based on the spectral-element method. For global simulations, we implemented a radially-symmetric Mars model with a 110 km thick crust (Sohl and Spohn 1997). For this 1D model, we successfully benchmarked the 3D seismic wave propagation solver SPECFEM3D_GLOBE (Komatitsch and Tromp 2002a,b) against the 2D axisymmetric wave propagation solver AxiSEM (Nissen-Meyer et al. 2014) at periods down to 10 s. We also present higher-resolution body-wave simulations with AxiSEM down to 1 s in a model with a more complex 1D crust, revealing wave propagation effects that would have been difficult to interpret based on ray theory. For 3D global simulations based on SPECFEM3D_GLOBE, we superimposed 3D crustal thickness variations capturing the distinct crustal dichotomy between Mars' northern and southern hemispheres, as well as topography, ellipticity, gravity, and rotation. The global simulations clearly indicate that the 3D crust speeds up body waves compared to the reference 1D model, whereas it significantly changes surface waveforms and their dispersive character depending on its thickness. We also perform regional simulations with the solver SES3D (Fichtner et al. 2009) based on 3D crustal models derived from surface composition, thereby addressing the effects of various distinct crustal features down to 2 s. The regional simulations confirm the strong effects of crustal variations on waveforms. We conclude that the numerical tools are ready for examining more scenarios, including various other seismic models and sources.

Keywords Body waves · computational seismology · crust · numerical methods · surface waves

1 Introduction

Knowledge of Earth's interior structure comes from geophysical analyses, and seismology in particular. However, due to the paucity of geophysical data bearing on the interiors of planets other than Earth (e.g., Lognonné and Johnson 2007), a significant part of our current knowledge of the mantle and bulk composition of Mars derives from geochemical analyses of a suite of basaltic achondrite meteorites that are believed to come from Mars (e.g., Dreibus and Wänke 1985; Treiman 1986; McSween 1994; Taylor 2013). In addition hereto, analysis of geodetic data obtained from ranging to orbiting and landed spacecraft (e.g. Folkner et al. 1997; Yoder et al. 2003; Neumann et al. 2004; Bills et al. 2005; Genova et al. 2016; Lainey et al. 2007; Konopliv et al. 2011, 2016) have enabled us to obtain a first-order picture of the gross interior structure of Mars.

This situation is expected to drastically change with the launch of the InSight (Interior Exploration using Seismic Investigations, Geodesy, and Heat Transport) mission (Banerdt et al. 2013), which has been selected by NASA to land a seismometer on the surface of Mars in November 2018. InSight is the first planetary mission dedicated to acquiring geophysical data from surface-installed instruments to explore the internal structure and dynamics

of a solar system object other than the Earth and the Moon. InSight will deploy a geophysical payload consisting of a single three-component Very Broad Band (VBB) seismometer (Seismic Experiment for Interior Structure, SEIS) (Lognonne et al. 2012; Mimoun et al. 2012; Lognonné and Pike 2015), a heat flow probe (Heat Flow and Physical Properties Probe, HP^3) (Spohn et al. 2014), and an experiment to conduct high-precision measurements of the rotation and orientation of Mars (Rotation and Interior Structure Experiement, RISE) (Folkner et al. 2012).

The goals of the mission are to provide insight on the formation and evolution of terrestrial planets by investigating the interior structure and processes of Mars. It will estimate the structure and composition of the crust, mantle and core, the thermal state of the interior, and measure the rate and distribution of internal seismic activity and meteorite impacts. To achieve this, InSight will make use of advanced single-seismometer analysis techniques that are currently applied on Earth, along with extremely precise measurements of variations in the spin axis of the planet, and the subsurface thermal gradient to provide the first direct measurements of the internal structure of Mars (see Panning et al. (2017) in this issue).

Various 1D radially-symmetric seismic models have been proposed for Mars (e.g. Okal and Anderson 1978; Mocquet et al. 1996; Sohl and Spohn 1997; Zharkov and Gudkova 2005; Verhoeven et al. 2005; Khan and Connolly 2008; Rivoldini et al. 2011) including 1D Q models (e.g., Lognonné and Mosser 1993; Zharkov and Gudkova 1997; Nimmo and Faul 2013; Khan et al. 2016). It is relatively straightforward to model wave propagation in such 1D models based on semi-analytical normal-mode theory (e.g., Gilbert 1971; Dahlen and Tromp 1998) or the recently developed iterative direct solution method (e.g., Al-Attar and Woodhouse 2008). This enabled the estimation of seismograms and amplitudes of normal modes, surface wave and long-period body waves in several past studies (see Lognonné and Mosser (1993) up to 10 sec and Lognonne et al. (1996) up to 20 sec). The detection of normal-mode frequencies will likely provide the best constraints on Mars interior, as noted by Bolt and Derr (1969), and require only the deployment of a single lander equipped with a broadband seismometer. The excitation amplitude of fundamental normal modes by marsquakes was investigated in more details, for instance, by Lognonne et al. (1996) and Gudkova and Zharkov (2004), who both concluded on the detection possibility for quakes with moments larger than 10^{17} Nm, but unfortunately only for Rayleigh modes with angular order larger than 25. Another single-station inversion technique, based on the location of quakes and structural inversion of surface waves, was more recently demonstrated by Panning et al. (2015), which will enable upper-mantle and crustal inversions for quakes with moments larger than 10^{15} Nm. All these studies suggest a Very Broad Band (VBB) instrument with resolution equal or better than 10^{-9} m/s^2/Hz$^{1/2}$ in the 0.01 Hz − 1 Hz bandwidth and a high dynamic range, mostly related to the large temperature variations expected on the Mars surface (see Lognonne et al. (1996); Hoolst et al. (2003) and Mimoun et al. (2017) in this issue). On the other hand, based on seismological experience on Earth, the crust has

a very strong effect on seismic waves, particularly on surface waves, which may be highly non-linear (Montagner and Jobert 1988; Bozdağ and Trampert 2008; Panning et al. 2010). On Earth, crustal thickness ranges from $\sim$7 km underneath oceans to $\sim$70 km underneath the deepest continents, and the average crustal thickness is about 24 km. In contrast, gravity and topography measurements from Mars suggest a significant crustal dichotomy between the northern and southern hemispheres, with crustal thickness varying from a few kilometers to more than 80 km (Neumann et al. 2004; Wieczorek and Zuber 2004).

Developments in numerical methods and high-performance computing have enabled unprecedented simulations of seismic wave propagation in realistic 3D models. Among many other numerical techniques, the spectral-element method is particularly well-suited for simulations of seismic wave propagation (Komatitsch and Tromp 2002a,b; Capdeville et al. 2003; Chaljub et al. 2003; Chaljub and Valette 2004; Peter et al. 2011). In this study, we explore the effects of 3D structural variations on waveforms using the spectral-element method for both global and regional simulations. Our motivation is to characterize seismic signals which we expect to receive from a single broad-band instrument onboard InSight. With this goal in mind, we perform 3D simulations with 3D crustal models using the global- and continental-scale solver SPECFEM3D_GLOBE (Komatitsch and Tromp 2002a,b), and the regional solver SES3D (Fichtner et al. 2009). 3D crustal effects on global long-period surface waves ($>$ 80 s) were previously investigated by Larmat et al. (2008) using 3D spectral-element simulations in the mantle coupled with normal modes (Capdeville et al. 2003). Our aim is to also simulate shorter-period waves, including effects due to topography and attenuation as well as ellipticity, rotation and self-gravitation. Capdeville and Marigo (2007) proposed homogenising complex structures using their long-wavelength-equivalents to efficiently take crustal effects into account in 3D simulations. For 3D global simulations, here we follow the procedure described in Tromp et al. (2010) and honor crustal thickness variations to better sample the crust for numerical accuracy and computational efficiency. In addition, we benchmark global simulations based on SPECFEM3D_GLOBE with simulations based on the 2.5D axisymmetric spectral-element solver AxiSEM (Nissen-Meyer et al. 2014). In all simulations we use marsquakes as seismic sources. Anticipated additional primary sources of seismic activity include meteorite impacts and dust storms (e.g., Teanby and Wookey 2011; Nakamura 2015), which may be modelled in subsequent studies using the solvers and models presented here. Since no marsquakes were unambiguously detected during the Viking mission (e.g., Anderson et al. 1977), current estimates allow for a relatively large range in Martian seismicity (e.g., Golombek et al. 1992; Knapmeyer et al. 2006; Lognonné and Johnson 2007; Teanby and Wookey 2011). In the "medium" catalogue by Knapmeyer et al. (2006), which is based on extensive mapping of compressional and extensional faults observed in the MOLA (Mars Orbiting Laser Altimeter) shaded relief maps, most events occur at depths well above 60 km (see also in this issue,

Ceylan et al. 2017). Such shallow marsquakes are used in all numerical simulations presented in this manuscript.

## 2 Numerical Simulations of Global Seismic Wave Propagation

In this section, we present simulations of global seismic wave propagation based on the spectral-element solver SPECFEM3D_GLOBE (Komatitsch and Tromp 2002a,b). To begin with, we use a 1D model of the interior structure of Mars devised by Sohl and Spohn (1997) (Model A with a 110 km crustal thickness), which hereafter we refer to as the Sohl & Spohn model. It agrees with geodesy observations and is based on plausible assumptions about Mars composition deduced from the analysis of the SNC meteorites. The main motivation for choosing Sohl & Spohn is its simplicity in terms of the number of layers, making it straightforward to adapt to SPECFEM3D_GLOBE by mimicking the implementation of the Preliminary Reference Earth Model, PREM (Dziewonski and Anderson 1981). We superimposed 3D crustal thickness variations onto the Sohl & Spohn model, together with Martian topography. Furthermore, we implemented ellipticity, rotation, and gravity (using the Cowling approximation) by adapting the appropriate parameters for Mars. We benchmarked SPECFEM3D_GLOBE against AxiSEM down to 10 s, but because we are interested in crustal effects, particularly on surface waves, we predominantly focus on simulations of waveforms down to 20 s. As mentioned in the introduction, in this study we considered only marsquakes as seismic sources.

2.1 1D model

Sohl and Spohn (1997) propose two different 1D Mars models, which are in overall agreement with regards to the locations of first-order discontinuities, but differ in crustal thickness, core radius, and the suggested ratio of the composition of minerals. Our main focus in this article is on the effects of crustal thickness variations on seismic waves. We chose the Sohl and Spohn (1997) model (Model A) with a 110 km-thick crust (the other one, Model B, has a crustal thickness of 250 km) and smaller-size liquid core with a radius of 1468 km (Model B has a radius of 1667 km). Based on analysis of the solar tidal deformation of Mars using MGS radio tracking data, Yoder et al. (2003) obtained a large value of the second-degree tidal Love number $k_2 \sim 0.15$, which implies the presence of a fluid core or at least of a liquid outer core (Khan and Connolly 2008; Rivoldini et al. 2011). The k_2 value has been confirmed in recent studies using additional tracking data from Mars Reconnaissance Orbiter, Mars Odyssey, and Mars Exploration Rover Opportunity (e.g., Lainey et al. 2007; Marty et al. 2009; Konopliv et al. 2011, 2016).

In its current form, SPECFEM3D_GLOBE requires a solid inner core for computational stability. Since inner-core shear waves are irrelevant, we added a solid inner core of pure fcc Fe with a radius of ~ 500 km to the Sohl & Spohn

model (Figure 1), rather than reconfiguring the entire 3D solver. Inner core density, compressional and shear wavespeeds were calculated under the relevant pressure and temperature conditions following Rivoldini et al. (2011). The resulting core model is mildly physically inconsistent because the pressure and temperature conditions inside the core of the Sohl & Spohn model do not allow for an inner core, and the total mass of the planet is slightly off. However, this solid inner core has absolutely no effect on synthetic seismograms, and its presence is irrelevant for the purposes of this study. We closely followed the implementation of PREM (Dziewonski and Anderson 1981), which is the main reference model for Earth simulations, and adapted the mesh to Mars by changing the radius and the number of spectral-elements in each domain appropriately, closely honoring first-order discontinuities such as the crust-mantle boundary, the upper-mantle discontinuities, the core-mantle boundary, etc. The mesh designed for NEX = 160, where NEX denotes the number of spectral elements along the surface of one side of each of the six chunks that constitute the cubed sphere (see Komatitsch and Tromp (1999) for details), is shown in Figure 1. Our comparisons with higher-resolution simulations with NEX = 256 and NEX = 320 show that NEX = 160 is able to resolve periods down to ~ 20 s (Figure 2). Our tests suggest that NEX = 256 is able to resolve ~ 15 s waves, and we can confidently go down to ~ 10 s with NEX = 320 simulations.
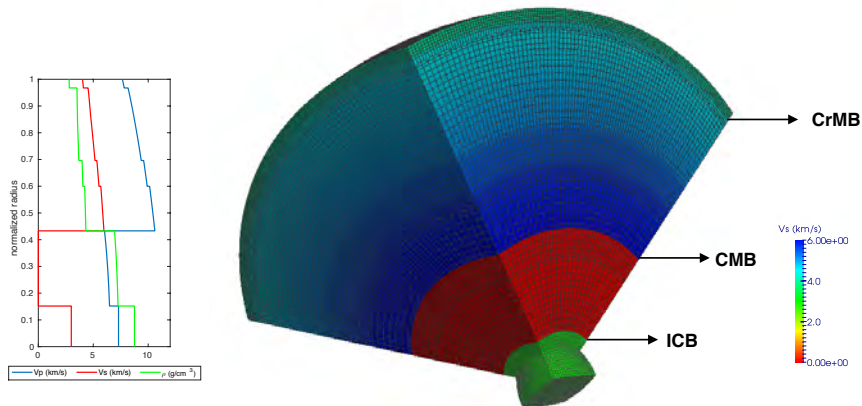
Fig. 1 *Left:* Reference 1D Mars model developed by Sohl and Spohn (1997). We added an inner core with a 515 km radius and calculated its density, compressional and shear wavespeeds under the relevant pressure and temperature conditions following Rivoldini et al. (2011). *Right:* Spectral-element mesh designed for the Sohl & Spohn model for NEX = 160, where NEX denotes the number of spectral elements along one side of one of the six chunks that represent the globe on the surface. CrMB, CMB and ICB denote crust-mantle, core-mantle and inner-core boundaries, respectively.
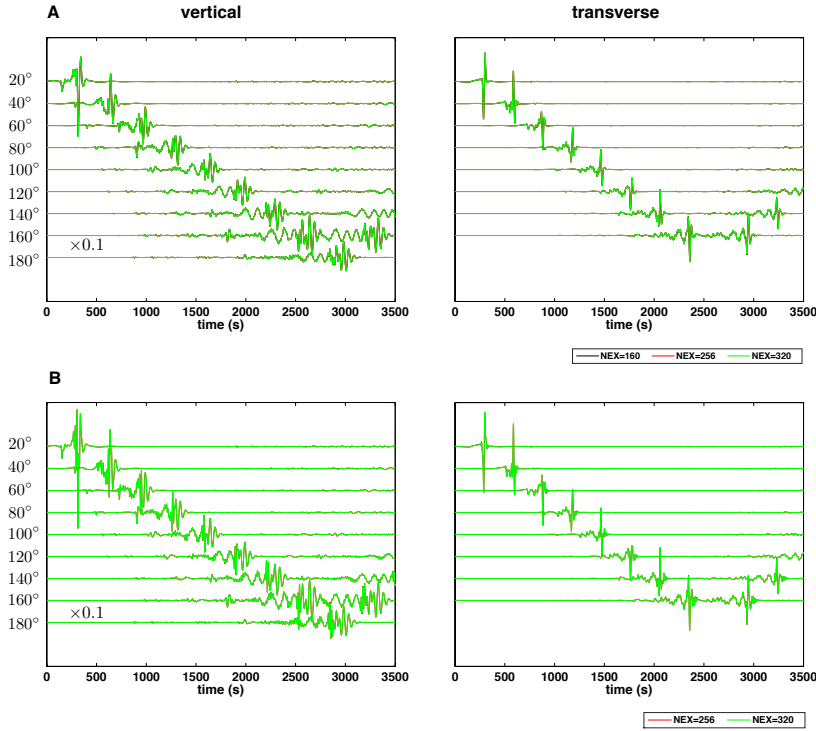
Fig. 2 Resolution of 1D simulations for various meshes with NEX = 160, 256, and 320, where NEX is the number of spectral elements along one side of each of the six chunks that constitute the cubed sphere on the surface. Seismograms are bandpassed between A) 20 s and 250 s, B) 15 s and 250 s, indicating that the NEX = 160 and NEX = 256 meshes resolve waves with a shortest period down to 20 s and 15 s, respectively. Vertical- and transverse-component seismograms show P, SV & Rayleigh waves and SH & Love waves, respectively. Antipodal seismograms are normalised by 10. Moment tensor solution of the 2011 Virginia earthquake (M_w = 5.8, depth = 12 km) is used as a source during simulations where the source and receivers are located along the equator with 20° epicentral distance spacing, as denoted on the left.

Following a similar strategy as for Earth, we implemented ellipticity with a flattening coefficient of 1/169.8 (Smith et al. 1999) by solving Clairaut's equation using Radau's approximation (Dahlen and Tromp 1998) (Figure 3). Self-gravitation is taken into account in SPECFEM3D_GLOBE based on the Cowling approximation (Cowling 1941), that is, the background gravitational potential is calculated based on the 1D density profile and density variations due to wave motion are ignored. We take viscoelasticity into account based on PREM attenuation values assigned to the corresponding layers of the 1D Sohl & Spohn model. In Figure 4 we show a comparison of synthetic seismograms computed using the Sohl & Spohn model with and without ellipticity, rotation, gravity, and attenuation. The duration of the seismograms is 150 min,

which is long enough to capture multi-orbit surface waves, such as R2, G2, R3, G3, and even G4 at some of the stations. The major discrepancy between the two sets of waveforms is due to attenuation, whereas rotation, ellipticity, and gravity are more important for long-period waves (see Komatitsch and Tromp (2002a) for a thorough analysis). The seismograms are computed for the moment-tensor solution of the 2011 Virginia Earthquake ($M_w = 5.8$, depth 12 km) located at $0°$ latitude and $0°$ longitude and recorded by a set of receivers located along the equator. They are band pass filtered between 20 s and 250 s, considering the resolution of the mesh and the limitations of the Cowling approximation.
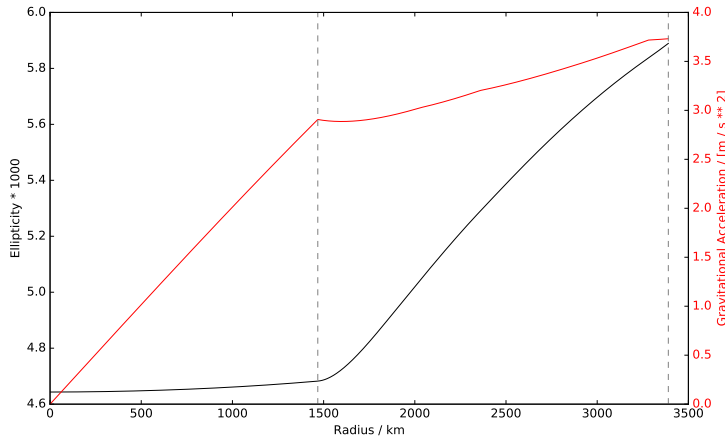
Fig. 3 Ellipticity and gravitational acceleration profiles of Mars. The flattening coefficient is 1/169.8 (Smith et al. 1999).

2.2 3D model

It is well known from Earth seismology that the crust has a strong influence on surface waves (e.g., Montagner and Jobert 1988; Bozdağ and Trampert 2008), but also on some body waves, such as SS (e.g., Ritsema et al. 2009). To this end, to assess the effects of 3D crustal variations on Martian seismograms, we superimposed 3D crustal thickness variations and topography onto the 1D Sohl & Spohn model; we refer to this as the Sohl & Spohn + 3DCrust model.

We first implemented topographic variations on top of the 1D reference model. The high-resolution topography is derived from the measurements of the Mars Orbiter Laser Altimeter (MOLA) (Smith et al. 1999) and the high-resolution planetocentric radii of the topographic model are reconstructed using spherical harmonics up to degree 2,600 (Wieczorek and Zuber 2004), which corresponds to a resolution of about 5 km. For our purposes, considering a shortest wave period of ~ 10 s, we truncated the spherical harmonic

expansion at degree 540, which gives a lateral resolution of about 20 km. For Earth simulations with SPECFEM3D_GLOBE, topography is implemented with respect to the hydrostatic reference ellipsoid, which is a good first-order approximation of the geoid. We used the same approach to implement Martian topography (Figure 5-A).

Second, we superimposed 3D crustal variations on top of the Sohl & Spohn model based on inversions of martian gravity and topography data (e.g., Neumann et al. 2004; Baratoux et al. 2014). As part of the InSight mission, a suite of new reference crustal thickness models for Mars has been constructed using a range of average crustal thicknesses and crustal and mantle densities (Plesa et al. 2016). For our simulations, we chose the model that used the mantle density profile derived from the compositional model of Wänke and Dreibus (1994) with a crustal density of 3,000 kg m^{-3} and a minimum crustal thickness of 10 km. This model has an average crustal thickness of 60 km. Following the implementation of 3D crustal model of CRUST2.0 (Bassin et al. 2000) used for Earth simulations in SPECFEM3D_GLOBE, we defined the Martian crust in terms of 5-layers, where shear and compressional wavespeeds are fixed to the average values of the reference model, 4.062 km/s and 7.732 km/s, respectively. The 3D crustal thickness map is defined on a $1° \times 1°$ grid. We implemented a smoothed version using a spherical harmonic expansion up to degree 20 (Figure 5-B). Following Tromp et al. (2010), crustal thickness is honored by the mesh using 1-to-5 spectral elements in the radial direction, depending on thickness. This allows us to optimise the speed of the simulations while accurately taking crustal variations and other 3D effects into account. The effects of Mars topography and crustal dichotomy have been previously investigated based on a spectral-element method coupled with a normal-mode method (CSEM) by Larmat et al. (2008). Their results show only slight differences between 1D and 3D seismograms, mainly because the simulations where performed at long periods, where surface waves are less sensitive to the crustal structure. With the possibility of access to broadband Mars seismograms via the InSight mission, we chose to go to much shorter periods in our 3D global simulations.

In Figure 6, we show sample cross-sections across Hellas Planitia and Olympus Mons & Arsia Mons, where the thinnest and thickest crustal thicknesses are observed, respectively. Note how crustal thickness variations are captured by the spectral-element mesh.

Figure 7 shows two snapshots of the vertical-component surface displacement wavefield from 3D simulations with topography and crustal variations. Distortions in the wavefield are clearly visible while propagating through Valles Marineris and Hellas Planitia, where crustal thickness and topography change significantly, for instance, in the form of a speed-up of surface waves as these traverse a region with thinner crust beneath Hellas Planitia as well as amplitude variation due to focusing and defocusing.

A comparison of 1D and 3D vertical- and transverse-component seismograms computed for the Sohl & Spohn and Sohl & Spohn + 3DCrust models, respectively, is presented in Figure 8 to show the effect of 3D crustal varia-

tions on waveforms azimuthally. Seismograms are filtered between 20 s and 250 s, where the effect of 3D variations becomes significant. We see clearly that the regions of Olympus Mons and Tharsis Montes, with crustal thicknesses larger than 80 km, generate large dispersive surface waves, particularly Rayleigh waves, compared to paths traversing thinner crustal regions due to focusing. These preliminary results give us a good indication of what kinds of signals we should expect from all azimuthal ranges around the location of the InSight seismometer.

2.3 AxiSEM and Instaseis: high-frequency synthetic seismograms for radially symmetric models

Despite the ever increasing computational power available, the $\mathcal{O}(\omega^4)$ complexity where ω is the highest resolved seismic frequency, of numerical full 3D wave propagation renders computation of synthetic seismograms with these methods impractical for high frequency body waves ($T < 5$ s) on the global scale. Still, synthetic data is crucial in preparation for data return from Mars, including the highest frequencies that are expected to be recorded for teleseismic events (around 1 Hz).

To overcome this problem, we use *Instaseis* (van Driel et al. 2015, www.instaseis.net) and *AxiSEM* (Nissen-Meyer et al. 2014, www.axisem.info), which work on axially symmetric models and reduce the computational complexity to $\mathcal{O}(\omega^3)$ by decomposing the 3D problem into a set of 2D problems. This decomposition also allows to store full 3D wavefields permanently and extract seismograms from these databases very quickly. Synthetics as continuous data with noise as well as Green's function generated this way are available at http://instaseis.ethz.ch, (see Ceylan et al. (this issue, 2017) for details).

Here, we highlight some of the effects that can be observed in these simulations for one particular model, see Figure 9(a) and Khan et al. (2016).

As the seismograms (Figure 9(b)) contain a wealth of phases, the correct phase identification turned out to be a major challenge in source location (Böse et al. 2017) as well as inversion for structure (Khan et al. 2016). The wavefields in Figure 10 may help to understand some of the complex wave propagation effects that are not easy to see in seismograms, e.g.:

Long coda: Especially S waves exhibit a long coda, even in this relatively simple 1D model. From the wavefields it can be seen that this is due to energy being trapped in the crust. The strength of this effect strongly depends on the velocity contrast at the Moho, which is relatively large in the model used here.

Complexity of the direct P waves: Even direct P waves appear with complex shapes in record sections, the wavefields reveal that this is due to reflections in the near source region.

2.4 Benchmark of numerical methods

To assess the stability of our numerical simulations, we benchmarked the results from SPECFEM3D_GLOBE and AxiSEM numerical packages for the 1D Sohl & Spohn model. We used the same earthquake mentioned in SPECFEM3D_GLOBE simulations section (2011 Virginia earthquake) and included attenuation. We plotted and compared the seismograms produced by these two packages recorded by a set of aligned receivers (Figure 11). The seismograms are filtered between 10 s and 250 s. The results from these two numerical techniques are in good agreement, suggesting the robustness of the numerical simulations presented here at least down to 10 s.

3 Regional waveform modeling: Influence of lateral and radial seismic crustal variations

In this section we focus on regional-scale simulations with lateral variations in crust-mantle topography and seismic properties (P and S wavespeed and density) using the SES3D package (Fichtner et al. 2009). We first briefly describe how 3D seismic wavespeed models are built, followed by a summary of the waveform modeling approach. SES3D is, like SPECFEM3D_GLOBE, based on a 3D spectral-element discretisation of the seismic wave equation. But, unlike SPECFEM3D, SES3D relies on a regular grid in spherical coordinates. For high-resolution imaging, this is disadvantageous, but has the advantage of relative ease of implementation and use. As a consequence, topographic variations cannot be implemented in SES3D. However, the purpose of the computations presented here is to obtain a first-order understanding of the effects of lateral variations in crustal seismic wavespeeds on seismic wave propagation.

3.1 Constructing three-dimensional seismic wavespeed models

In constructing 3D seismic wavespeed models of the Martian crust, we follow Baratoux et al. (2014) and consider the surface concentrations of the oxides of the major elements (CaO, FeO, MgO, Al_2O_3, and SiO_2) measured by the Mars Odyssey gamma-ray spectrometer (GRS) as representative of crustal composition. This is undoubtedly a questionable assumption given that igneous rocks at Gusev crater, the major element composition of Martian meteorites, and modeling studies of mineral assemblages that result from low-pressure crystallization of primary melts of the primitive mantle all point to a more complex scenario (e.g., Taylor 2013). In view of the purpose of this study – modeling wave propagation in laterally heterogeneous media – this potential limitation is less significant, as long as the order of magnitude of the heterogeneities is correct. Prior to waveform modeling, the compositional maps were linearly extrapolated on a finer grid and subsequently rescaled to a smaller region (see below for more details) to ensure that the models were smooth, thus usable for

SEM simulations. Further details on the construction of the maps are given in Metthez (2016).

To convert the surface compositions derived by Baratoux et al. (2014) to physical properties (seismic wave velocities and density), we employ a thermodynamic method based on Gibbs free energy minimization (www.perplex.ethz.ch/). Gibbs energy minimization is a technique by which mantle mineralogy, and its elastic properties, can be predicted as a function of pressure, temperature, and bulk composition from thermodynamic data (e.g., Connolly 2009). This methodology is currently being used extensively as a means of putting seismological constraints on the mantle composition of the Earth and the terrestrial planets (e.g., Kuskov et al. 2006; Khan and Connolly 2008; Khan et al. 2014; Rivoldini et al. 2011; Drilleau et al. 2013). For the purposes of the present study, we assume mantle composition to be constant throughout the model and use the bulk compositional estimate of Dreibus and Wänke (1985). The thermodynamic code assumes isotropy in computed seismic wave velocities.

In addition to composition, we also require pressure and temperature to compute physical properties. The mantle pressure profile was obtained by integrating the vertical load from the surface pressure boundary condition. Within the lithosphere, temperature was computed by using a prescribed smooth geothermal gradient to a depth of 100 km after Khan and Connolly (2008), whereas the sublithospheric mantle adiabat was defined by the entropy of the lithology at a temperature of 1200 K, i.e., at the base of the lithosphere. Added hereto, is the crustal thickness model obtained from analysis of Mars Global Surveyor gravity and topography data (Neumann et al. 2004; Wieczorek and Zuber 2004). This model is shown in Figure 12 and includes for reference the region studied here (framed box). Crustal thickness is seen to vary between 10 and 120 km across the study region and bears evidence of the crustal dichotomy. Finally, as shear-wave attenuation model we employ the Q model of Nimmo and Faul (2013) for a grain size of 1 cm. As an illustration of computed properties for this model, shear-wave velocities are shown in Figure 13. Extracted 1D profiles across the region show the resultant variation in shear wavespeeds throughout the model. These comprise variations of ~5% in the upper ~20 km, while variations across the Moho, including an intra-crustal mineralogical transition at around 60 km depth, are seen to encompass ~15–20%.

For comparison, we have also constructed a model with crustal dichotomy. This model is also shown in Figure 13 and has been constructed in the same manner as the model without the dichotomy, except that the part in the crust related to the dichotomy was tailored for this purpose by subtracting small random components in all physical properties. As a consequence, this model is unlikely to bear any relationship to the actual Martian crust, but this is less significant in the present context of wanting to investigate effects of lateral variation on wave propagation.

3.2 Waveform modeling

To solve the wave equation in our regional Mars models with lateral variations in seismic properties, we use SES3D (Fichtner et al. 2009). Perfectly matched layers are implemented to avoid reflections from unphysical boundaries of the spherical section. The Martian models considered here contain discontinuities associated with the Moho and an intra-crustal mineralogical phase change. A requirement for spectral-element solutions is that discontinuities coincide with the edges of elements. Because of the regular grid of SES3D, however, discontinuities in material properties may sometimes be located inside an element. As a result, the numerical solutions may be slightly inaccurate relative to perfectly honored discontinuities, but we deem this inconsequential given that the vertical extent of an element size is typically less than the resolution of the crustal thickness model.

The lateral extent of the region considered here is $90\times90°$ (figure 12A). However, to keep the computational cost of modeling waveforms down to 2 s within reasonable limits, we shrunk the framed region shown in figure 12A to $20\times20°$ (figure 12B). Based on a minimum shear-wave speed of 3.6 km/s, dominant period of 2 s, lateral model extensions of $\sim$1200 km and 400 km in depth, respectively, and two spectral elements per wavelength, the physical modeling domain consists of 360×112 cells. Also, since each spectral element consists of 5 GLL points, final resolution improves by a factor of $\sim$4. The source time function contains periods from 2 s up to 100 s. The source used here for illustration is a small $M_w = 2.98$ ($2.95\cdot10^{10}$ Nm) from the catalog of Ceylan et al. (2017). Similar events are contained in the "medium" catalogue by Knapmeyer et al. (2006). With this set-up, we compute synthetic high-frequency ($\sim$2 s) seismograms at various distances from the above event, as described below.

3.3 Results

Synthetic seismograms computed for the source described above at an epicentral distance of 16.2° are shown in Figure 14. In this figure we compare seismograms computed using the radial (1D) and three-dimensional (3D) models shown earlier (Figure 13), in addition to a composite model (1D/3D Moho) consisting of a 1D crustal velocity component and a 3D crustal thickness component. In the case of 3D models, these include crustal models with and without dichotomy. To show more details, only the first part of the traces right after the main P- and S-wave arrivals are shown. Theoretically-predicted arrival times of some major P- and S-wave phases are also shown. These were computed using the TauP toolkit (Crotwell et al. 1999) based on the "1D" model (black bold line in Figure 13E).

From the computed waveforms we can make the following two observations: 1) travel time differences for the direct P-wave arrival are insignificant and generally <1-2 s for the S-wave arrival. To first order, this implies that

location errors based on purely radial models relative to those relying on more complex models, are minor. This is an important observation in that current marsquake location algorithms in the context of InSight work on the premise of 1D models (e.g., Panning et al. 2015; Böse et al. 2017; Khan et al. 2016); 2) significant waveform differences in both amplitude and phase for seismic phases arriving after the main P-wave arrival are present. In particular, the biggest distinction occurs between model "1D" and the other two models, but strong variations are also seen to occur between "1D/3D" and "3D". As expected, large differences in amplitude and phase are also seen to be present between models with and without dichotomy. This analysis suggests that both crustal thickness and lateral velocity variations affect the seismic waveforms of body and surface waves.

Effects of lateral velocity variations and crustal thickness on wave propagation is illustrated further in Figure 15, which shows variation in computed seismograms (vertical component) for models "1D" and "3D" in the epicentral distance range ~2°–18° along a line to the North-East of the station (see Figure 12). As the epicentral distance increases, and therefore the variety of structure sampled, the difference between "1D" and "3D" clearly becomes larger. In line herewith, comparison of "3D" seismograms for models with and without dichotomy are also distinguishable. While the seismograms are clearly path dependent and show significant variation, particularly in secondary arrivals, the onset of P-wave and S-wave arrivals for the "1D" and "3D" models are similar. This underlines the point made earlier that locations based on spherically symmetric models will effectively be equivalent to locations that rely on more complex models. Effects of variations in lateral structure and crustal thickness might become important, however, for later arriving seismic phases that are expected to be used as a means of iteratively refining any initial structure models. This approach has been applied to synthetic Martian seismograms by Khan et al. (2016), where, after an initial inversion based on surface-wave dispersion data and P- and S-wave travel times, additional phases (e.g., pP, sP, PP, PPP, sS, SS, and SSS) are picked and employed in a subsequent inversion as a means of further refining structure and parameters related to event location. Differences between later arrivals (e.g., PP) based on 1D and 3D models amount to a couple of seconds (Figure 14), which is capable of introducing errors in the resultant models. The solution here would be to operate with more advanced means of computing travel times that are capable of accounting for e.g., the aspherical nature of the planet, crustal thickness variations, and lateral variations in seismic properties.

4 Discussions & Conclusions

In this study we demonstrated the effects of 3D structure, particularly the crust, on Martian waveforms to assess what kind of signals we should expect from a single seismometer to be deployed within the InSight mission. We used SPECFEM3D_GLOBE for 3D simulations and presented seismograms having

resolution down to 20 s, accommodating 3D crustal thickness variations, topography, attenuation, gravity, ellipticity, and rotation. For 1D models, AxiSEM provides an alternative way to simulate high-resolution body waves down to 1 s. In addition, we demonstrated more detailed crustal models in regional simulations capturing variations also of wavespeeds and density derived from mineralogical models with the SES3D code. Both global and regional simulations illustrate the significant effect of 3D structure on waveforms, which is essential to analyse the first seismic signals from Mars. We showed that various numerical solvers are now available to analyse the interior of Mars further in terms of waveform modeling which will be complementary to the modelling techniques with a single-instrument presented in Panning et al. (2017) to discern the complexity of Martian seismograms. In addition 3D seismic wave simulations offer opportunities to test and calibrate the source and structural inversion techniques before applying them to the observed Martian seismograms. Future studies will consider other proposed models, both elastic and anelastic, for Mars, for instance, to address the proposed low-wavespeed zone in upper mantle. We are now at a stage to explore the effect of different seismic sources such as meteorite impacts in addition to marsquakes which could be a major source of seismic signals generated on Mars. For regional simulations we also plan to take the topography into account in future studies which is likely to affect the regional waveforms around 5 s.

References

D. Al-Attar, J.H. Woodhouse, Calculation of seismic displacement fields in self-gravitating earth modelsapplications of minors vectors and symplectic structure. gji **175(3)**, 1176–1208 (2008). doi:10.1111/j.1365-246X.2008.03961.x

D.L. Anderson, W.F. Miller, G.V. Latham, Y. Nakamura, M.N. Toksoz, A.M. Dainty, F.K. Duennebier, A.R. Lazarewicz, R.L. Kovach, T.C.D. Knight, Seismology on mars. J. Geophys. Res. **82**, 4524–4546 (1977)

W.B. Banerdt, S. Smrekar, P. Lognonné, T. Spohn, S.W. Asmar, D. Banfield, L. Boschi, U. Christensen, V. Dehant, W. Folkner, D. Giardini, W. Goetze, M. Golombek, M. Grott, T. Hudson, C. Johnson, G. Kargl, N. Kobayashi, J. Maki, D. Mimoun, A. Mocquet, P. Morgan, M. Panning, W.T. Pike, J. Tromp, T. van Zoest, R. Weber, M.A. Wieczorek, R. Garcia, K. Hurst, InSight: A Discovery Mission to Explore the Interior of Mars, in *Lunar and Planetary Science Conference*. Lunar and Planetary Inst. Technical Report, vol. 44, 2013, p. 1915

D. Baratoux, H. Samuel, C. Michaut, M.J. Toplis, M. Monnereau, M. Wieczorek, R. Garcia, K. Kurita, Petrological constraints on the density of the martian crust. Journal of

Geophysical Research: Planets **119**(7), 1707–1727 (2014). doi:10.1002/2014JE004642. http://dx.doi.org/10.1002/2014JE004642

C. Bassin, G. Laske, G. Masters, The current limits of resolution for surface wave tomography in North America, in *EOS*, vol. F897, 2000, p. 81

B.G. Bills, G.A. Neumann, D.E. Smith, M.T. Zuber, Improved estimate of tidal dissipation within Mars from MOLA observations of the shadow of Phobos. Journal of Geophysical Research (Planets) **110**, 7004 (2005). doi:10.1029/2004JE002376

B.A. Bolt, J.S. Derr, Free bodily vibrations of the terrestrial planets. Vistas in Astronomy **11(1)**, 69–102 (1969)

M. Böse, J. Clinton, S. Ceylan, F. Euchner, M. van Driel, A. Khan, D. Giardini, A Probabilistic framework for single-station location of seismicity on Earth and Mars. Phys. Earth Planet Sci. **262**, 48–65 (2017)

E. Bozdağ, J. Trampert, On crustal corrections in surface wave tomography. Geophy. Journal. Int., 1066–1082 (2008). doi: 10.1111/j.1365-246X.2007.03690.x

Y. Capdeville, J.-J. Marigo, Second order homogenization of the elastic wave equation for non-periodic layered media. Geophys. J. Int., 823–838 (2007). doi: 10.1111/j.1365-246X.2007.03462.x

Y. Capdeville, E. Chaljub, J.P. Vilotte, J.P. Montagner, Coupling the spectral element method with a modal solution for elastic wave propagation in global earth models. gji **152**, 34–67 (2003)

S. Ceylan, M. van Driel, F. Euchner, A. Khan, J. Clinton, L. Krischer, M. Böse, D. Giardini, From initial models of seismicity, structure and noise to synthetic seismograms for Mars. Space Sci Rev this volume (2017). submitted

E. Chaljub, B. Valette, Spectral element modelling of three-dimensional wave propagation in a self-gravitating Earth with an arbitrarily stratified outer core. Geophys. J. Int. **158**, 131–141 (2004)

E. Chaljub, Y. Capdeville, J.P. Vilotte, Solving elastodynamics in a fluid-solid heterogeneous sphere: a parallel spectral-element approximation on non-conforming grids. J. Comput. Phys. **187**(2), 457–491 (2003)

J.A.D. Connolly, The geodynamic equation of state: What and how. Geochemistry, Geophysics, Geosystems **10**(10), (2009). Q10014. doi:10.1029/2009GC002540

T.G. Cowling, The non-radial oscillations of polytropic stars. Mon. Not. Roy. Astron. Soc. **101**, 369–373 (1941)

H.P. Crotwell, T.J. Owens, J. Ritsema, The taup toolkit: Flexible seismic travel-time and ray-path utilities. Seismological Research Letters **70**(2), 154–160 (1999). doi:10.1785/gssrl.70.2.154

F.A. Dahlen, J. Tromp, *Theoretical Global Seismology* (Princeton Univ. Press,, Princeton, NJ, USA, 1998)

G. Dreibus, H. Wänke, Mars, a volatile-rich planet. Meteoritics **20**, 367–381 (1985)

M. Drilleau, . Beucler, A. Mocquet, O. Verhoeven, G. Moebs, G. Burgos, J.-P. Montagner, P. Vacher, A bayesian approach to infer radial models of temperature and anisotropy in the transition zone from surface wave dispersion curves. Geophysical Journal International **195**(2), 1165–1183 (2013). doi:10.1093/gji/ggt284. http://gji.oxfordjournals.org/content/195/2/1165.abstract

A.M. Dziewonski, D.L. Anderson, Preliminary reference earth model. Physics of the Earth and Planetary Interiors **25**(4), 297–356 (1981). doi:http://dx.doi.org/10.1016/0031-9201(81)90046-7. http://www.sciencedirect.com/science/article/pii/0031920181900467

A. Fichtner, B.L.N. Kennett, H. Igel, H.-P. Bunge, Full seismic waveform tomography for upper-mantle structure in the Australasian region using adjoint methods. Geophysical Journal International **179**, 1703–1725 (2009)

W.M. Folkner, C.F. Yoder, D.N. Yuan, E.M. Standish, R.A. Preston, Interior structure and seasonal mass redistribution of mars from radio tracking of mars pathfinder. Science **278**(5344), 1749–1752 (1997). doi:10.1126/science.278.5344.1749. http://science.sciencemag.org/content/278/5344/1749

W.M. Folkner, S.W. Asmar, V. Dehant, R.W. Warwick, The rotation and interior structure experiment (RISE) for the InSight mission to Mars, in *43rd Lunar and Planetary Science Conference, Lunar and Planetary Inst.*, Houston, TX, 2012, p. 1721. http://www.lpi.usra.edu/meetings/lpsc2012/pdf/1721.pdf

A. Genova, S. Goossensc, F.G. Lemoineb, E. Mazaricob, G.A. Neumannb, D.E. Smitha, M.T. Zubera, Seasonal and static gravity field of Mars from MGS, Mars Odyssey and MRO radio science. Icarus **272**, 228–245 (2016)

F. Gilbert, Excitation of normal modes of the earth by earthquake sources. Geophys. J. R. astr. Soc. **22**, 223–226 (1971)

M.P. Golombek, W.B. Banerdt, T.L. Tanaka, D.M. D. M. Tralli, A prediction of mars seismicity from surface faulting. Science **258**, 979–981 (1992)

T.V. Gudkova, V.N. Zharkov, Mars: interior structure and excitation of free oscillations. pepi **142**, 1–22 (2004)

T.V. Hoolst, V. Dehant, F. Roosbeek, P. Lognonné, Tidally induced surface displacements, external potential variations, and gravity variations on Mars. Icarus **161**, 281–296 (2003)

A. Khan, J.A.D. Connolly, Constraining the composition and thermal state of Mars from inversion of geophysical data. Journal of Geophysical Research (Planets) **113**, 7003 (2008). doi:10.1029/2007JE002996

A. Khan, J.A.D. Connolly, A. Pommier, J. Noir, Geophysical evidence for melt in the deep lunar interior and implications for lunar evolution. Journal of Geophysical Research (Planets) **119**, 2197–2221 (2014). doi:10.1002/2014JE004661

A. Khan, M. van Driel, M. Böse, D. Giardini, S. Ceylan, J. Yan, J. Clinton, F. Euchner, P. Lognonné, N. Murdoch, D. Mimoun, M. Panning, M. Knapmeyer, W.B. Banerdt, Single-station and single-event marsquake location and inversion for structure using synthetic martian waveforms. Physics of the Earth and Planetary Interiors **258**, 28–42 (2016). doi:http://dx.doi.org/10.1016/j.pepi.2016.05.017. http://www.sciencedirect.com/science/article/pii/S0031920116300875

M. Knapmeyer, J. Oberst, E. Hauber, M. Wählisch, C. Deuchler, R. Wagner, Working models for spatial distribution and level of Mars' seismicity. J. Geophys. Res. E Planets **111**(11), 1–23 (2006). ISBN 0148-0227. doi:10.1029/2006JE002708

D. Komatitsch, J. Tromp, Introduction to the spectral element method for three-dimensional seismic wave propagation. Geophysical Journal International **139**(3), 806–822 (1999). doi:10.1046/j.1365-246x.1999.00967.x. http://doi.wiley.com/10.1046/j.1365-246x.1999.00967.x

D. Komatitsch, J. Tromp, Spectral-element simulations of global seismic wave propagation-I. Validation. Geophysical Journal International **149**(2), 390–412 (2002a). doi:10.1046/j.1365-246X.2002.01653.x. http://doi.wiley.com/10.1046/j.1365-246X.2002.01653.x

D. Komatitsch, J. Tromp, Spectral-element simulations of global seismic wave propagation II . Three-dimensional models , oceans , rotation and self-gravitation. Geophysical Journal International **150**(1), 303–318 (2002b). doi:10.1046/j.1365-246X.2002.01716.x. http://doi.wiley.com/10.1046/j.1365-246X.2002.01716.x

A.S. Konopliv, R.S. Park, W.M. Folkner, An improved {JPL} mars gravity field and orientation from mars orbiter and lander tracking data. Icarus **274**, 253–260 (2016). doi:http://dx.doi.org/10.1016/j.icarus.2016.02.052. http://www.sciencedirect.com/science/article/pii/S0019103516001305

A.S. Konopliv, S.W. Asmar, W.M. Folkner, zgr Karatekin, D.C. Nunes, S.E. Smrekar, C.F. Yoder, M.T. Zuber, Mars high resolution gravity fields from mro, mars seasonal gravity, and other dynamical parameters. Icarus **211**(1), 401–428 (2011). doi:http://dx.doi.org/10.1016/j.icarus.2010.10.004. http://www.sciencedirect.com/science/article/pii/S0019103510003830

O.L. Kuskov, V.A. Kronrod, H. Annersten, Inferring upper-mantle temperatures from seismic and geochemical constraints: Implications for kaapvaal craton. Earth and Planetary Science Letters **244**(12), 133–154 (2006). http://www.sciencedirect.com/science/article/pii/S0012821X06001403

V. Lainey, V. Dehant, M. Pätzold, First numerical ephemerides of the Martian moons. Astron. Astrophys. **465**, 1075–1084 (2007). doi:10.1051/0004-6361:20065466

C. Larmat, J.-P. Montagner, Y. Capdeville, W.B. Banerdt, P. Lognonné, Numerical assessment of the effects of topography and crustal thickness on martian seismograms using a coupled modal solution-spectral element method. Icarus **196**, 78–89 (2008)

P. Lognonné, C. Johnson, 10.03 - Planetary Seismology, in *Treatise on Geophysics*, ed. by G. Schubert (Elsevier, Amsterdam, 2007), pp. 69–122. ISBN 978-0-444-52748-6. doi:http://dx.doi.org/10.1016/B978-044452748-6.00154-1

P. Lognonné, B. Mosser, Planetary seismology. Surv. Geophys. **14(3)**, 239–302 (1993)

P. Lognonné, W.T. Pike, Planetary seismometry. Extraterrestrial Seismology, 3–3648 (2015). doi:10.1017/CBO9781107300668.006

P. Lognonne, J.G. Beyneix, W.B. Banerdt, S. Cacho, J.F. Karczewski, M. Morand, Ultra broad band seismology on intermarsnet. Planet. Space Sci. **44**, 1237–1249 (1996)

P. Lognonne, W.B. Banerdt, K. Hurst, D. Mimoun, R. Garcia, M. Lefeuvre, J. Gagnepain-Beyneix, M. Wieczorek, A. Mocquet, M. Panning, E. Beucler, S. Deraucourt, D. Giardini, L. Boschi, U. Christensen, W. Goetz, T. Pike, C. Johnson, R. Weber, C. Larmat, N. Kobayashi, J. Tromp, Insight and Single-Station Broadband Seismology: From Signal and Noise to Interior Structure Determination., in *Lunar and Planetary Institute Science Conference Abstracts*, vol. 43, 2012, p. 1493

J.C. Marty, G. Balmino, J. Duron, P. Rosenblatt, S.L. Maistre, A. Rivoldini, V. Dehant, T.V. Hoolst, Martian gravity field model and its time variations from {MGS} and odyssey data. Planetary and Space Science **57**(3), 350–363 (2009). doi:http://dx.doi.org/10.1016/j.pss.2009.01.004. http://www.sciencedirect.com/science/article/pii/S0032063309000178

H.Y. McSween Jr., What we have learned about Mars from SNC meteorites. Meteoritics **29**, 757–779 (1994)

N. Metthez, *Analysing effects of heterogeneities on Martian synthetic waveforms using full waveform and thermodynamic modeling* (MSc Thesis, ETH Z "urich, 2016)

D. Mimoun, P. Lognonne, W.B. Banerdt, K. Hurst, S. Deraucourt, J. Gagnepain-Beyneix, T. Pike, S. Calcutt, M. Bierwirth, R. Roll, P. Zweifel, D. Mance, O. Robert, T. Nebut, S. Tillier, P. Laudet, L. Kerjean, R. Perez, D. Giardini, U. Christenssen, R. Garcia, The InSight SEIS Experiment, in *Lunar and Planetary Institute Science Conference Abstracts*, vol. 43, 2012, p. 1493

D. Mimoun, N. Murdoch, P. Lognonne, W.T. Pike, K. Hurst, the SEIS Team, The seismic noise model of the insight mission to mars. Space Sci Rev this volume (2017)

A. Mocquet, P. Vacher, O.G.C. Sotin, Theoretical seismic models of mars: The importance of the iron content of the mantle. Planet. Space Sci. **44(11)**, 1251–1268 (1996)

J. Montagner, N. Jobert, Vectorial tomography – II. Application to the Indian Ocean. grl **94**, 309–344 (1988)

Y. Nakamura, Planetary seismology: Early observational results. Extraterrestrial Seismology, 3–3648 (2015). doi:10.1017/CBO9781107300668.006

G.A. Neumann, M.T. Zuber, M.A. Wieczorek, P.J. McGovern, F.G. Lemoine, D.E. Smith, Crustal structure of mars from gravity and topography. Journal of Geophysical Research: Planets **109**(E8) (2004). E08002. doi:10.1029/2004JE002262

F. Nimmo, U.H. Faul, Dissipation at tidal and seismic frequencies in a melt-free, anhydrous Mars. Journal of Geophysical Research (Planets) **118**, 2558–2569 (2013). doi:10.1002/2013JE004499

T. Nissen-Meyer, M. van Driel, S. Stähler, K. Hosseini, S. Hempel, L. Auer, A. Colombi, A. Fournier, AxiSEM: broadband 3-D seismic wavefields in axisymmetric media. Solid Earth **5(1)**, 425–445 (2014). doi:10.5194/se-5-425-2014

E.A. Okal, D.L. Anderson, Theoretical models for mars and their seismic properties. Icarus **33**, 514–528 (1978)

M.P. Panning, V. Lekić, B. Romanowicz, Importance of crustal corrections in the development of a new global model of radial anisotropy. jgr **115**, 12325 (2010)

M.P. Panning, É. Beucler, M. Drilleau, A. Mocquet, P. Lognonné, W.B. Banerdt, Verifying single-station seismic approaches using Earth-based data: Preparation for data return from the InSight mission to Mars. Icarus **248**, 230–242 (2015). doi:10.1016/j.icarus.2014.10.035

M. Panning, P. Lognonne, B.W. Banerdt, R. Garcia, M. Golombek, S. Kedar, B. Knapmeyer-Endrun, A. Mocquet, N.A. Teanby, J. Tromp, R. Weber, E. Beucler, J.-F. Blanchette-Guertin, E. Bozdağ, M. Drilleau, T. Gudkova, S. Hempel, A. Khan, V. Lekic, N. Murdoch, A.-C. Plesa, A. Rivoldini, N. Schmerr, Y. Ruan, O. Verhoeven, C. Gao, U. Chris-

tensen, J. Clinton, V. Dehant, D. Giardini, D. Mimoun, W.T. Pike, S. Smrekar, M. Wieczorek, M. Knapmeyer, J. Wookey, Planned products of the Mars Structure Service for the mission to Mars. Space Sci Rev this volume (2017)

D. Peter, D. Komatitsch, Y. Luo, R. Martin, N. Le Goff, E. Casarotti, P. Le Loher, F. Magnoni, Q. Liu, C. Blitz, T. Nissen-Meyer, P. Basini, J. Tromp, Forward and adjoint simulations of seismic wave propagation on fully unstructured hexahedral meshes. Geophysical Journal International **186**(2), 721–739 (2011). doi: 10.1111/j.1365-246X.2011.05044.x. http://doi.wiley.com/10.1111/j.1365-246X.2011.05044.x

A.-C. Plesa, M. Grott, N. Tosi, D. Breuer, T. Spohn, M.A. Wieczorek, How large are present-day heat flux variations across the surface of mars? J. Geophys. Res. Planets **121**, 2386–2403 (2016). doi: 10.1002/2016JE005126

J. Ritsema, H.-J. van Heijst, J.H. Woodhouse, A. Deauss, Long-period body-wave travel-times through the crust: Implication for crustal corrections and seismic tomography. Geophy. Journal. Int **179**, 1255–1261 (2009). doi: 10.1111/j.1365246X.2009.04365.x, 2009

A. Rivoldini, T. Van Hoolst, O. Verhoeven, A. Mocquet, V. Dehant, Geodesy constraints on the interior structure and composition of Mars. Icarus **213**, 451–472 (2011). doi:10.1016/j.icarus.2011.03.024

D.E. Smith, M.T. Zuber, S.C. Solomon, R.J. Phillips, J.W. Head, J.B. Garvin, W.B. Banerdt, D.O. Muhleman, G.H. Pettengill, G.A. Neumann, F.G. Lemoine, J.B. Abshire, O. Aharonson, C. Brown David, S.A. Hauck, A.B. Ivanov, P.J. McGovern, H.J. Zwally, T.C. Duxbury, The global topography of mars and implications for surface evolution. Science **284**(5419), 1495–1503 (1999). doi:10.1126/science.284.5419.1495. http://science.sciencemag.org/content/284/5419/1495

F. Sohl, T. Spohn, The interior structure of mars: Implications from snc meteorites. Journal of Geophysical Research: Planets **102**(E1), 1613–1635 (1997). doi:10.1029/96JE03419. http://dx.doi.org/10.1029/96JE03419

T. Spohn, M. Grott, S. Smrekar, C. Krause, T.L. Hudson, the HP3 instrument team, Measuring the martian heat using the heat and physical properties package (HP3), in *45th Lunar and Planetary Science Conference*, Lunar and Planetary Inst., Houston, TX, 2014, p. 1916. http://www.hou.usra.edu/meetings/lpsc2014/pdf/1916.pdf

G.J. Taylor, The bulk composition of Mars. Chemie der Erde / Geochemistry **73**, 401–420 (2013). doi:10.1016/j.chemer.2013.09.006

N.A. Teanby, J. Wookey, Seismic detection of meteorite impacts on mars. Phys. Earth Planet. Inter. **186**, 70–80 (2011)

A.H. Treiman, The parental magma of the Nakhla achondrite: Ultrabasic volcanism on the shergottite parent body. Geochimica et Cosmochimica Acta **50**, 1061–1070 (1986). doi:doi:10.1016/0016-7037(86)90388-1

J. Tromp, D. Komatitsch, V. Hjörleifsdóttir, Q.L.H. Zhu, D. Peter, E. Bozdag, D. McRitchie, P. Friberg, C. Trabant, A. Hutko, Near real-time simulations of global CMT earthquakes. Geophy. J. Int. **183**, 381–389 (2010). doi: 10.1111/j.1365-246X.2010.04734.x

M. van Driel, L. Krischer, S.C. Stähler, K. Hosseini, T. Nissen-Meyer, Instaseis: instant global seismograms based on a broadband waveform database. Solid Earth **6**(2), 701–717 (2015). doi:10.5194/se-6-701-2015

S.D. Vance, S. Kedar, S.C. Stähler, R.D. Lorenz, M.P. Panning, B.G. Bills, H.-H. Huang, W.T. Pike, J. Castillo-Rogez, P. Lognonné, V.C. Tsai, A.R. Rhoden, Vital Signs: Seismology of ocean worlds. Astrobiology (2016). submitted

O. Verhoeven, A. Rivoldini, P. Vacher, A. Mocquet, G. Choblet, M. Menvielle, V. Dehant, T. Van Hoolst, J. Sleewaegen, J.-P. Barriot, P. Lognonné, Interior structure of terrestrial planets: Modeling Mars' mantle and its electromagnetic, geodetic, and seismic properties. Journal of Geophysical Research (Planets) **110**, 4009 (2005). doi:10.1029/2004JE002271

H. Wänke, G. Dreibus, Chemistry and accretion of Mars. Philos. Trans. R. Soc. London **A349**, 2134–2137 (1994)

M.A. Wieczorek, M.T. Zuber, Thickness of the martian crust: Improved constraints from geoid-to-topography ratios. Journal of Geophysical Research: Planets **109**(E1) (2004). E01009. doi:10.1029/2003JE002153

R. Yamada, P.L. R. F. Garcia, N. Kobayashi, N. Takeuchi, T. Nebut, H. Shiraishi, M. Calvet, J. Gagnepain-Beyneix, On the possibility of lunar core phase detection using new seismometers for soft-landers in future lunar missions. Planet. Space Sci. **81**, 18–31 (2013). doi: 10.1016/j.pss.2013.03.009

C.F. Yoder, A.S. Konopliv, D.N. Yuan, E.M. Standish, W.M. W. M. Folkner, Fluid core size ofmars from detection of the solar tide. Science **300(5617)**, 299–303 (2003)

V.N. Zharkov, T.V. Gudkova, Planetary seismology. Planet. Space Sci. **45(4)**, 401–407 (1997)

V.N. Zharkov, T.V. Gudkova, Construction of martian interior model. Solar System Research **39(5)**, 343–373 (2005)

P - SV - Rayleigh

SH - Love
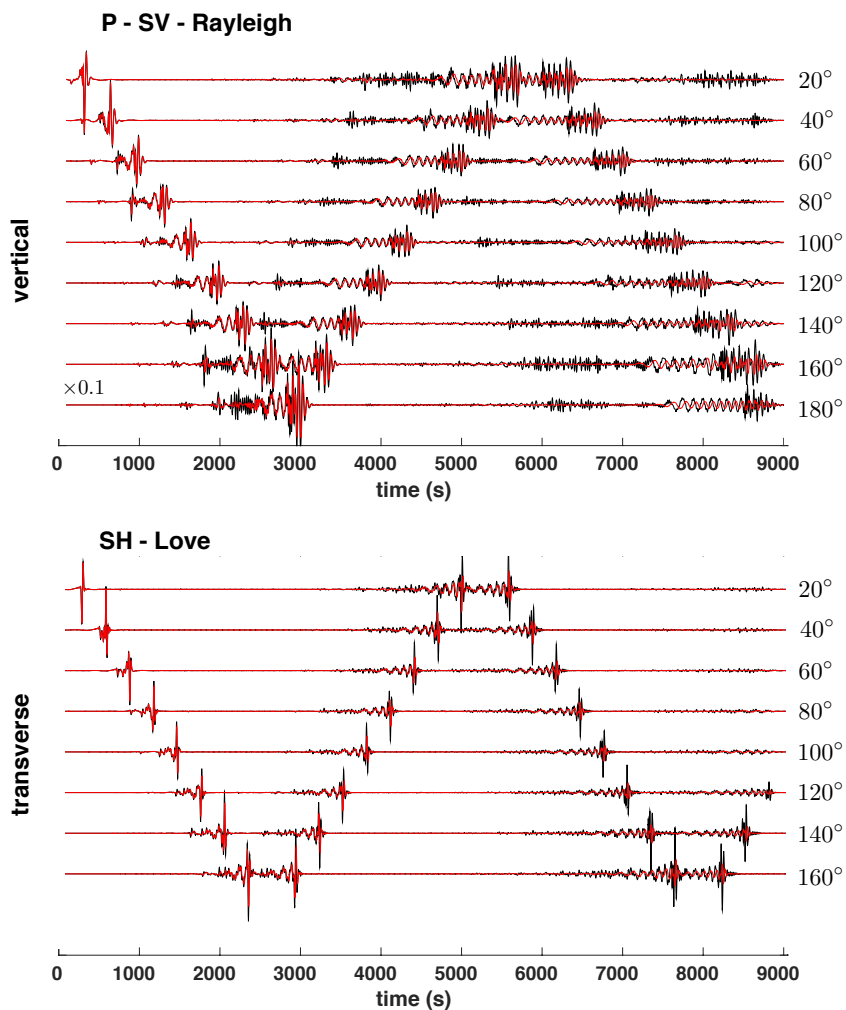
Fig. 4 Vertical- and transverse-component displacement seismograms computed for the 1D Sohl & Spohn model showing both minor- and major-arc seismic waves. Red and black seismograms are with and without attenuation/ellipticity/rotation/gravity, respectively. Moment tensor solution of the 2011 Virginia earthquake ($M_w = 5.8$, depth = 12 km) is used as a source during simulations where the source and stations are located along the equator with 20° epicentral distance spacing, as denoted on the right. Antipodal seismograms are normalised by 10 and all seismograms are filtered between 20 s and 250 s. Maximum amplitudes in the vertical and transverse seismic traces are $1.5 \cdot 10^{-5}$ and $1.7 \cdot 10^{-5}$ meters, respectively, excluding the antipodal seismograms.
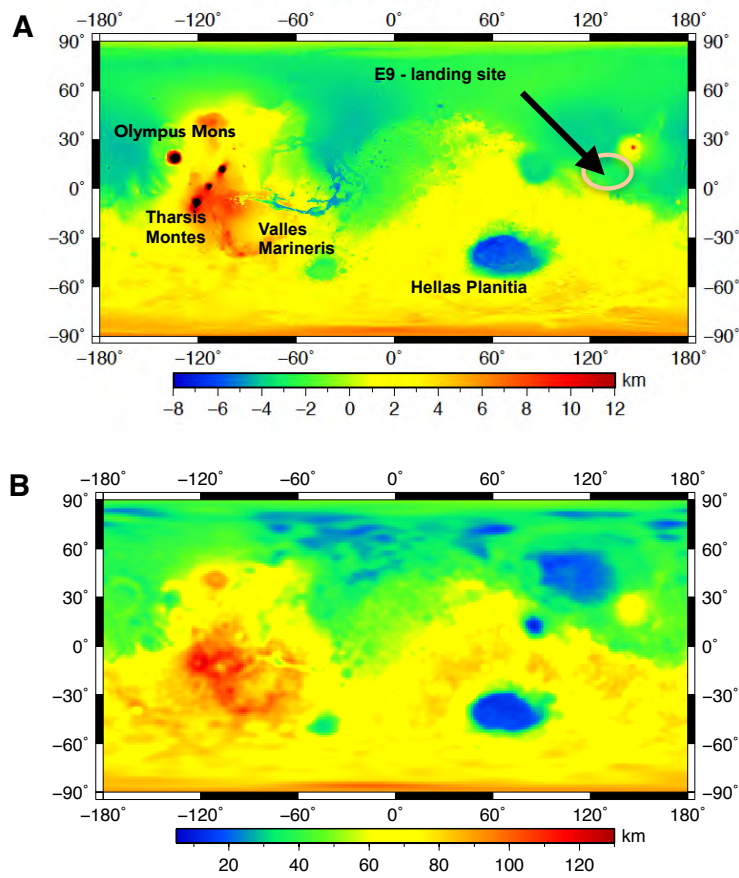
Fig. 5 A) Topography of Mars. The data are compiled from Mars orbiters (Wieczorek and Zuber 2004). B) Moho variations of Mars estimated from gravity data by assuming a constant crustal density (Wieczorek and Zuber 2004). In SPECFEM3D_GLOBE, smoothed versions of topography and crustal variations are implemented using spherical harmonic expansions up to degree 540 and degree 20, respectively.
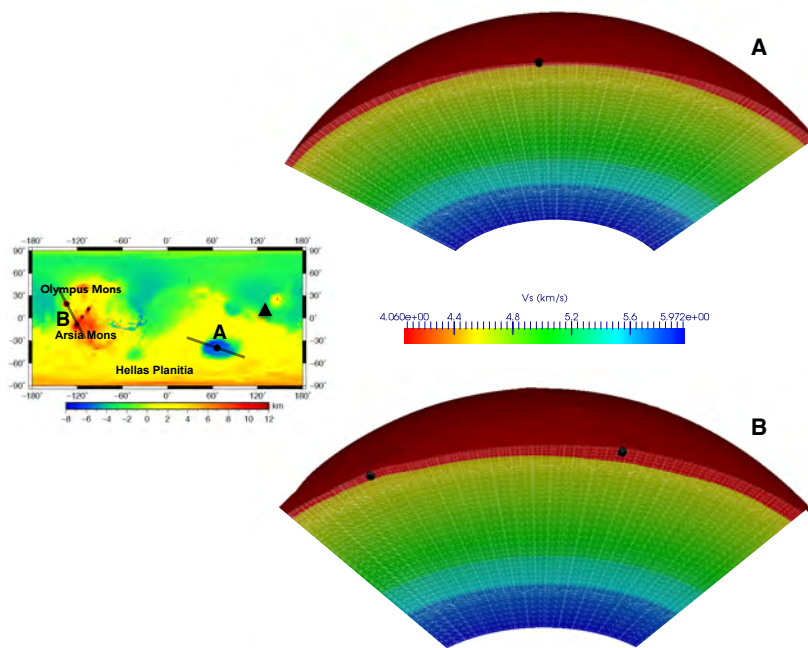
Fig. 6 Sample cross-sections of the mesh used to capture 3D crustal variations A) across Hellas Planitia, B) from Arsia Mons to Olympus Mons. The sections are denoted by grey lines on the topographic map on the left. Black dots on the cross-sections denote the centre of Hellas Planitia, Olympus Mons, and Arsia Mons. The black triangle in the map denotes the landing site.
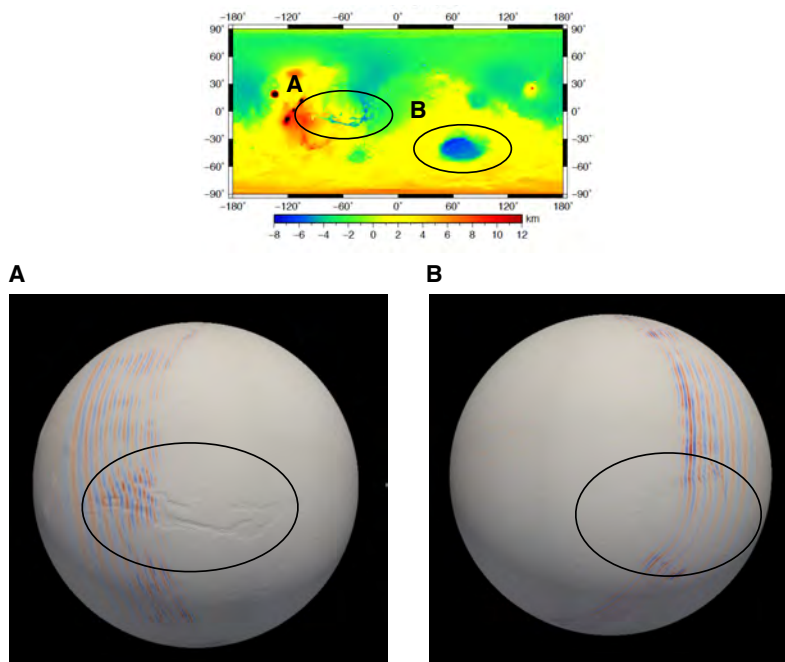
Fig. 7 Movie snapshots of wave propagation in the 3D crustal model through A) Valles Marineris and B) Hellas Planitia. The top map shows topographic variations.
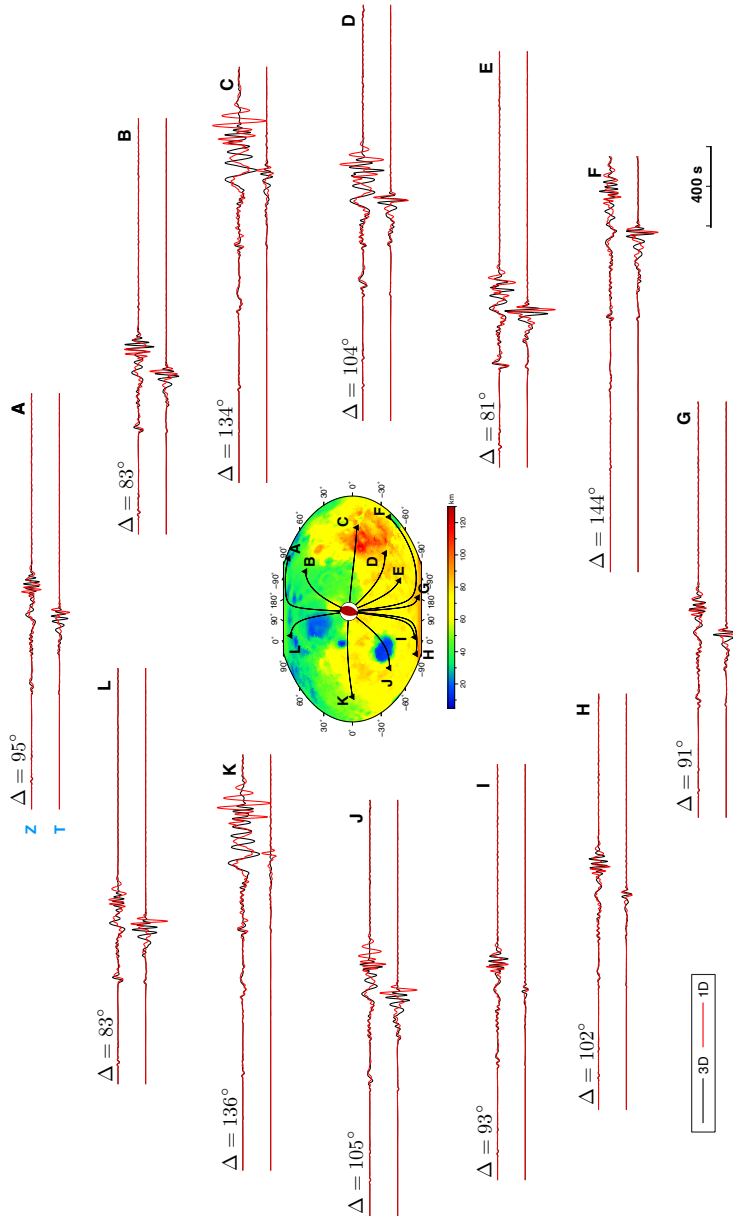
Fig. 8 Comparison of vertical (Z) and transverse (T) components of 1D (red) & 3D (black) seismograms computed for the Sohl & Spohn and Sohl & Spohn + 3DCrust models, respectively. Ellipticity, rotation, gravity, and attenuation were included in the simulations. In addition, topography was added to the Sohl & Spohn + 3DCrust model. Epicentral distances of source-receiver pairs are given at the top of the associated seismograms. For computational efficiency, the earthquake (2011 Virginia earthquake, $M_w = 5.8$, depth $= 12$ km) is located at the location of the single instrument to be deployed on the Mars surface, and stations are at possible locations of seismic sources. Note that due to source excitation in the 3D model and rotational effects reciprocal simulations may differ slightly. The map in the middle shows crustal thickness variations, station & source locations, and ray paths. Vertical- and transverse- component seismograms are normalised by their maximum displacements of $7.2 \cdot 10^{-6}$ and $2.1 \cdot 10^{-5}$ meters, respectively.
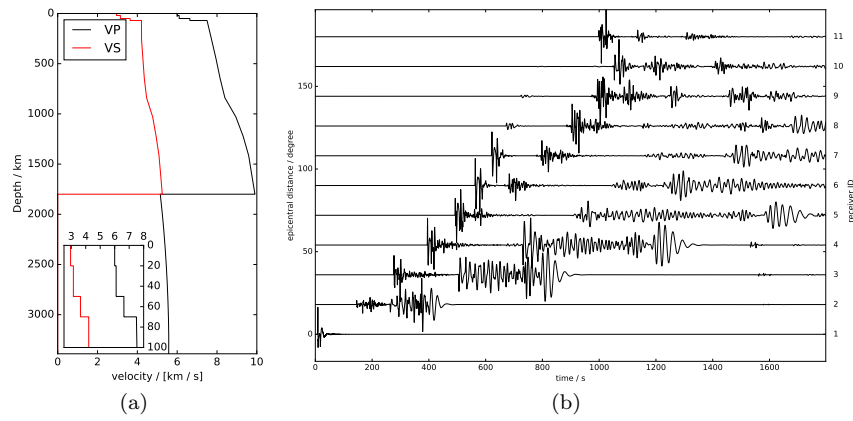
Fig. 9 (a) The seismic wavespeed model used in the AxiSEM simulations. The inset shows a zoom-in of crustal structure. (b) 30 min record section of vertical component seismograms filtered between $1-20$ s to an epicentral distance of $180°$. A vertical dipole source $(M_w = 3.9)$ located at a depth 52 km is used during the simulations. The receivers correspond to the locations marked with triangles in Figure 10.
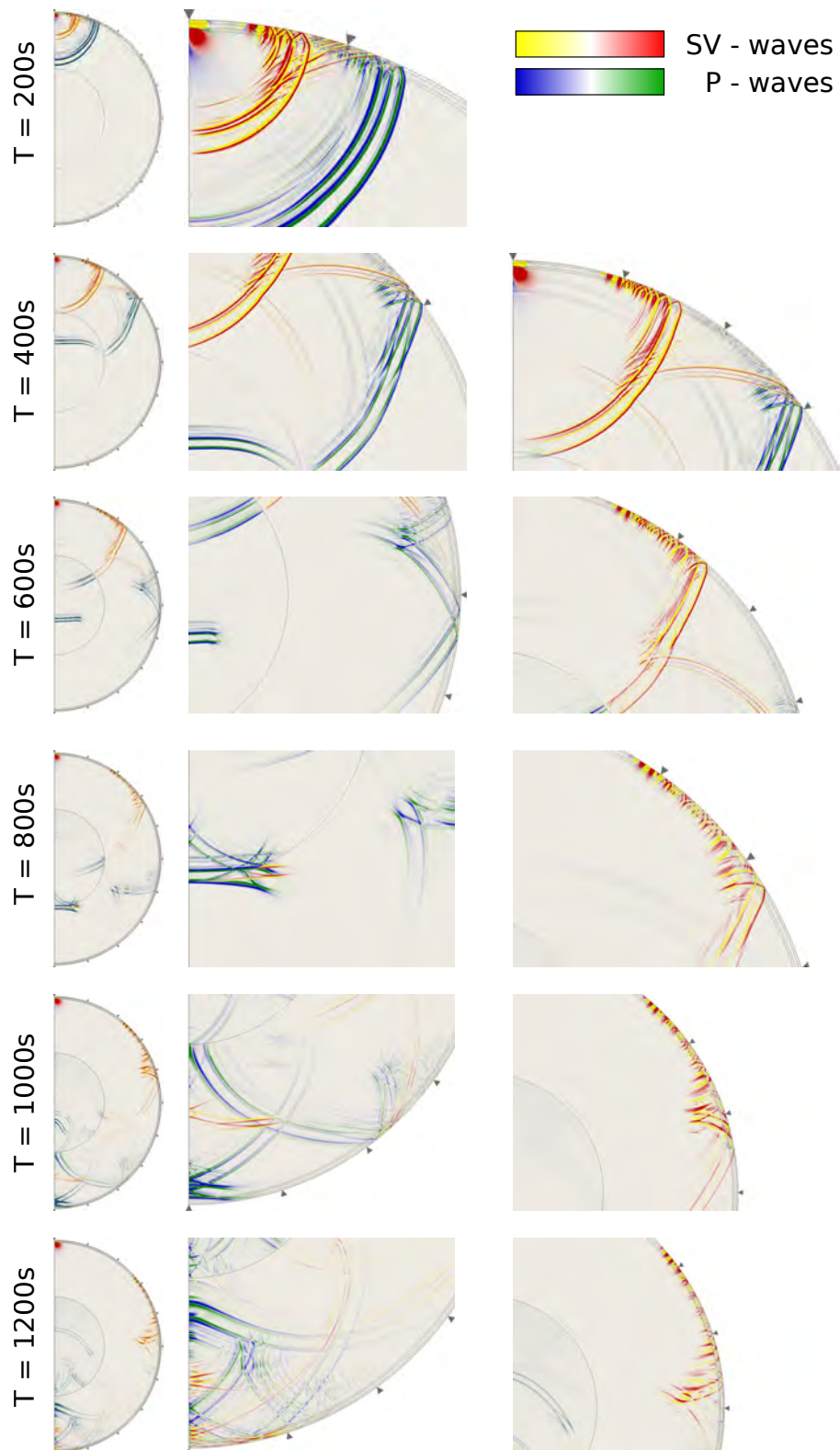
Fig. 10 Seismic waves propagating through Mars for a vertical dipole ($M_w = 3.9$) source at 52 km depth. T denotes time after the event in seconds, the first column of snapshots provides an overview while the others zoom into the interesting regions. P and S waves are indicated with different colorscales and are computed as the dilation and rotation in the vertical plane. The triangles mark the receivers used in the record section in Figure 9.
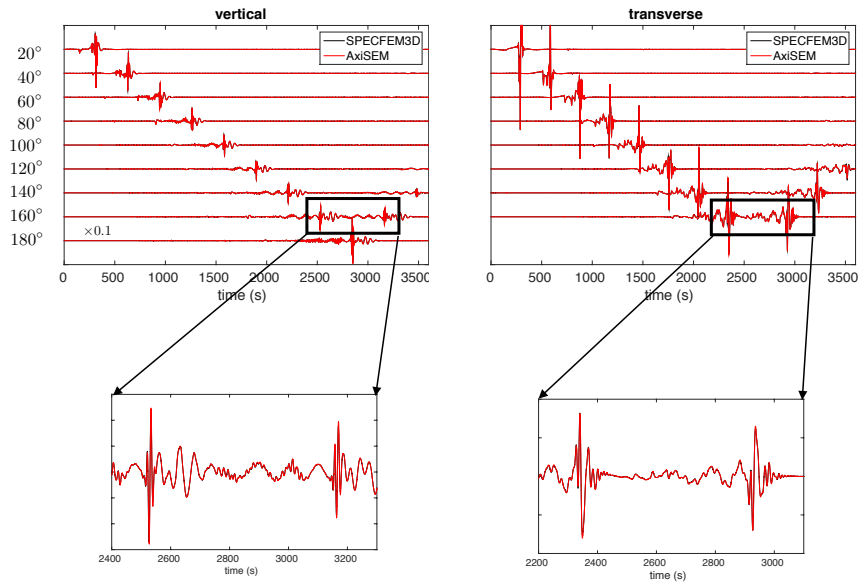
Fig. 11 Comparison of 1D numerical simulations from SPECFEM3D_GLOBE and AxiSEM for the Sohl & Spohn model. The seismograms are filtered between 10 s and 250 s. Epicentral distances are shown on the left and antipodal seismograms are scaled by 10. Moment tensor solution of the 2011 Virginia earthquake ($M_w = 5.8$, depth = 12 km) is used as a source during simulations where the source and receivers are located along the equator.
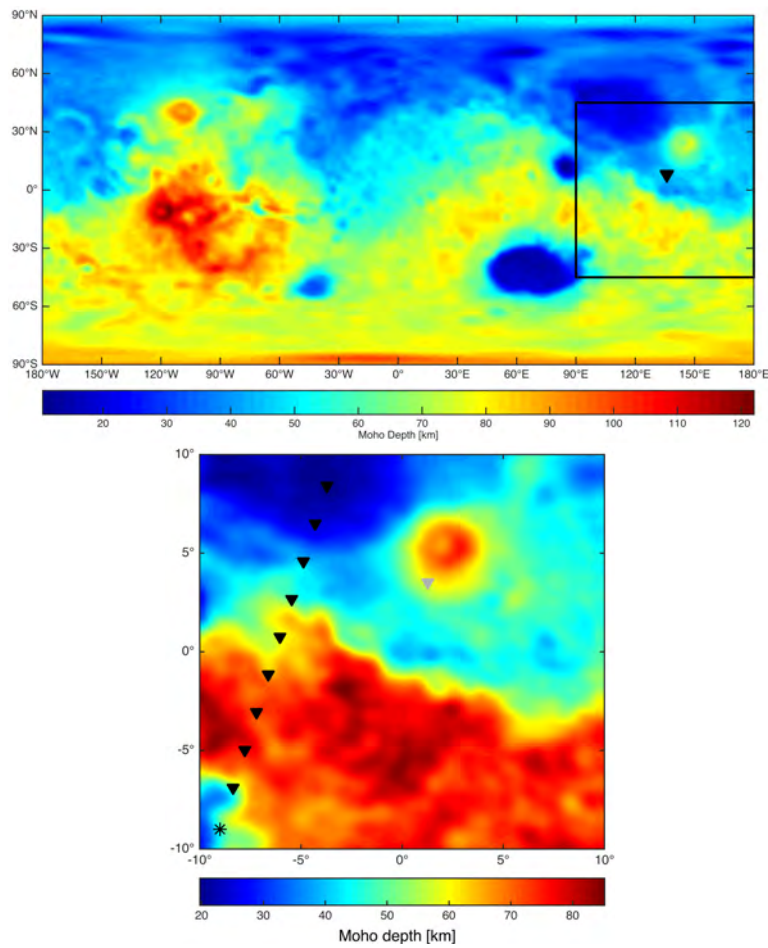
Fig. 12 Global (top) and regional (bottom) Martian crustal thickness map based on the models from Neumann et al. (2004) and Wieczorek and Zuber (2004). The region studied is indicated by the framed square in the top-most plot where the location of InSight is indicated by the inverted triangle. The plot on the right is a zoom-in of the framed region on the global map showing various locations of InSight (inverted triangles) for modeling different epicentral distances to the seismic event (star), which is located in the left-hand corner. The inverted gray triangle toward the middle of the plot indicates the location of the InSight seismometer at an epicentral distance of 16.2° from the event (see main text and Figure 14 for further information).
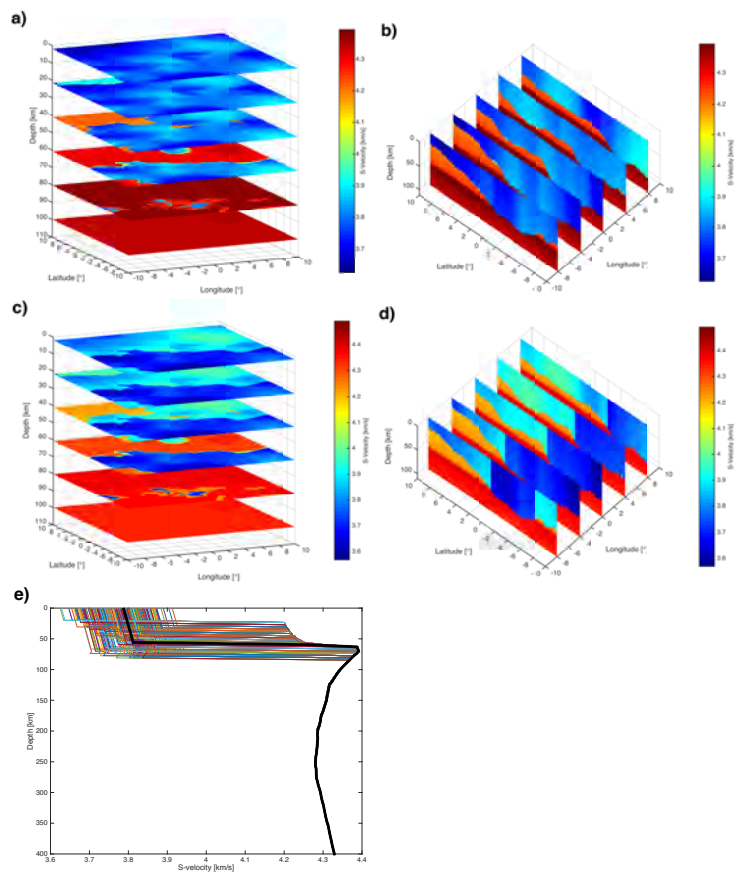
Fig. 13 Computed crust and mantle shear-wave velocities. Shown are slices through two models: without (A–B) and with (C—D) crustal dichotomy. Plots A and C show depth slices through the models, whereas plots B and D depict slices in longitude through the models. Plot E shows one-dimensional profiles gathered from all sub-regions of the model without dichotomy (A and B). The thick black line represent the one-dimensional model which has been constructed by averaging all of the regional one-dimensional models. The mantle component underneath all models is assumed one-dimensional.
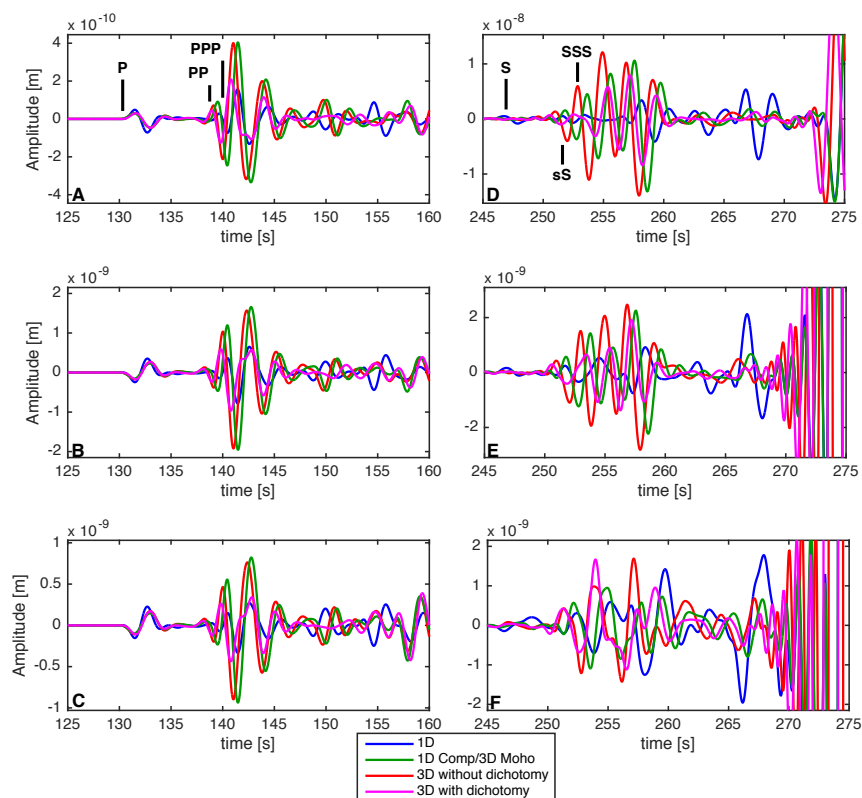
Fig. 14 Three-component (A–Radial; B–Transverse; C–Vertical) synthetic seismograms computed at an epicentral distance of 16.2° to the North-East of the event (inverted gray triangle in figure 12) using four different models. Model "1D" represents the one-dimensional model shown in figure 13E (black bold line); "1D/3D" (not shown) is a composite model consisting of a 1D crustal velocity component and a three-dimensional (3D) crustal thickness component; "3D" represent the three-dimensional models without (Figure 13A–B) and with crustal dichotomy (Figure 13C–D). A number of P-wave phases based on the "1D" model are indicated for reference. The mantle component underneath all models is assumed to be one-dimensional. Seismograms have been filtered between 2–100 s using a third-order Butterworth filer. The event is a double-couple ($M_w = 2.98$) located at a depth of 3 km.
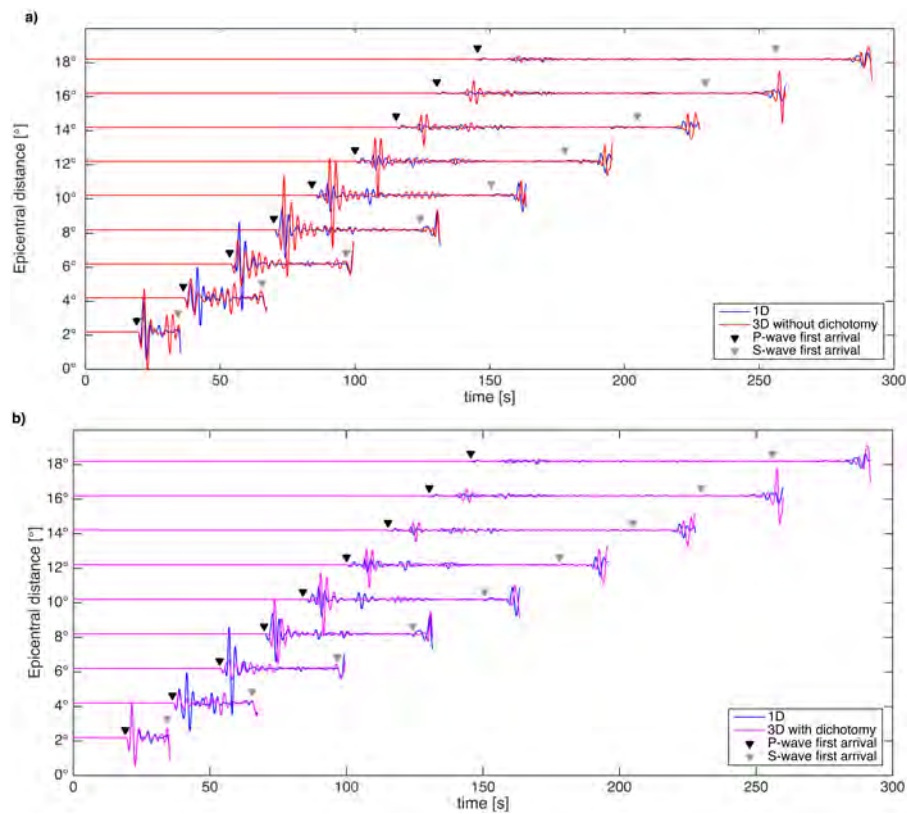
Fig. 15 Comparison of synthetic vertical-component seismograms for models without (A) and with (B) crustal dichotomy as a function of epicentral distance along a line North-East of the event (indicated by inverted black triangles in Figure 12). Seismograms have been filtered between 2–100 s using a third-order Butterworth filter. Theoretically predicted P-wave and S-wave first arrivals based on a "1D" model (black bold line in Figure 13E) are indicated for reference. Traces have been cut right before the arrival of the surface waves to enhance body wave arrivals. The event is a double-couple ($M_w = 2.98$) located at a depth of 3 km.